communications materials

Article

https://doi.org/10.1038/s43246-024-00713-y

Tuning a magnetic energy scale with pressure and field in UTe_2

Hyunsoo Kim [1,2] ✉, I-Lin Liu[2], Wen-Chen Lin[2], Yun Suk Eo [2,5], Sheng Ran[2,6], Nicholas P. Butch[2,3] & Johnpierre Paglione [2,4] ✉

When a fragile ordered state is suppressed to zero temperature, a quantum phase transition occurs, which is often marked by the appearance of unconventional superconductivity. While the quantum critical point can be hidden, the influence of the quantum criticality extends to fairly high temperatures, manifesting non-Fermi liquid behavior in a wide range of the field-temperature-pressure phase space. Here, we report the tuning of a magnetic energy scale in the heavy-fermion superconductor UTe_2, previously identified with a peak in the *c*-axis electrical transport temperature dependence, using applied hydrostatic pressures and *a*-axis-oriented magnetic fields as complementary (and opposing) tuning parameters: the characteristic peak in *c*-axis resistivity decreases in temperature with applied pressure before vanishing near the critical pressure of 15 kbar (1.5 GPa), while the application of field shifts the peak to a higher temperature and broadens it under all studied pressures. At the critical pressure, the transport behavior deviates from Fermi liquid behavior, exhibiting a nearly linear temperature dependence of resistivity with an enhanced pre-factor. Our results shed light on the microscopic origin of the *c*-axis resistivity peak and provide a clear picture of magnetic energy scale evolution relevant to quantum criticality in UTe_2.

Few systems in nature exhibit a fragile long-range magnetic order, where the thermal phase transition into its ordered state can be readily suppressed by either chemical substitution, magnetic field, or physical pressure. However, systems have been found, that undergo a quantum phase transition at a critical value of the tuning parameter[1–4], deemed a quantum critical point (QCP). But the QCP is often putative, being hidden within a surrounding superconducting phase which is thought to be mediated by fluctuations affiliated with the magnetic order[1]. While the majority of magnetic unconventional superconductors are found near an antiferromagnetic instability, several uranium-based superconductors including URhGe and UCoGe coexist with ferromagnetism[5], making them promising candidates for a topological spin-triplet superconductivity[6].

Recently, UTe_2 was identified as a new member of the U-based superconductor family[6], with a transition temperature T_c reaching up to 2 K[7]. The normal state of UTe_2 can be described by the Kondo lattice model where the localized magnetic moment of uranium is hybridized with the conduction electrons at low temperatures[8]. UTe_2 does not magnetically order at ambient pressure, but the superconductivity in this paramagnetic heavy-fermion material is believed to be in the vicinity of a magnetic instability[6]. The application of pressures above 15 kbar (1.5 GPa) has shown signatures of magnetism[9] which have recently been confirmed as long-range antiferromagnetic order[10]. Because of the relatively small energy scales of the superconductivity and magnetic order in UTe_2, a rich phase diagram emerges when the system is subjected to external parameters, not unlike similar phase diagrams in many strongly correlated systems including heavy-fermion[11], cuprate[12], and iron-based[13] superconductors. However, an intricate understanding of the competition and interplay between magnetism and superconductivity in UTe_2 remains elusive, and the associated quantum criticality in the *H*-*p*-*T* phase space has not been fully explored.

In UTe_2, electrical resistivity exhibits the behavior of a Fermi liquid in its temperature dependence above T_c for currents applied along all three crystallographic axes[14]. Whereas the resistivity along the *a*- and *b*-axis directions is consistent with typical incoherent-to-coherent crossover phenomena upon cooling as expected for a Kondo lattice at low temperatures, Eo et al.[14] found a qualitatively different behavior in the *c*-axis transport which exhibits a pronounced local maximum around 12 K. An anomaly in $d\rho_a/dT$[14,15] (ρ_a stands for resistivity with $I||a$) and χ_a (magnetic susceptibility with $H||a$)[16] was reported at the same temperature. The

[1]Department of Physics, Missouri University of Science and Technology, Rolla, MO, USA. [2]Maryland Quantum Materials Center, Department of Physics, University of Maryland, College Park, MD, USA. [3]NIST Center for Neutron Research, National Institute of Standards and Technology, Gaithersburg, MD, USA. [4]Canadian Institute for Advanced Research, Toronto, ON, Canada. [5]Present address: Department of Physics and Astronomy, Texas Tech University, Lubbock, TX, USA. [6]Present address: Department of Physics, Washington University in St. Louis, St. Louis, MO, USA. ✉e-mail: hyunsoo.kim@mst.edu; paglione@umd.edu

pressure evolution of χ_a was studied by Li et al.[16], which exhibits a clear inflection point that moves to lower temperatures with increasing applied pressure. In contrast, χ_b exhibits a broad local maximum of around 35 K, and its pressure evolution is scaled with that of the metamagnetic transition field[17]. A similar peak in the electrical transport measurement was identified at 16 K in an unoriented sample[18] and in a sample under applied pressure[9]. Other measurements – including heat capacity[15], linear thermal expansion coefficient[19], nuclear magnetic resonance[20], and thermoelectric power[21] – also exhibit a prominent feature near 12 K, a temperature scale which has been associated with a magnetic energy scale of ~1 meV based on thermodynamic measurements[15]. While there are varying views on the nature of magnetic fluctuations and their observation in UTe_2[22–24], previous studies consistently point to this energy scale as being magnetic in origin, allowing the tracking of this feature in *c*-axis transport to be used as a unique tool to study the evolution of the magnetic fluctuation spectrum in UTe_2.

Transport properties of UTe_2 have been studied under various orientations of pressure and field[9,17,25]. In this work, we study its transport properties in a unique configuration with $I \| c$ and $H \| a$ where pressure- and field-tuning of the magnetic energy scale provide insight into the role of magnetism in unconventional superconductivity in UTe_2. Furthermore, we elucidate the presence of quantum criticality in its rich phase diagram. By performing precision measurements of the electrical resistance R under applied pressures up to 17.4 kbar and in magnetic fields up to 18 T, we determine the pressure and field evolution of the characteristic magnetic energy scale, upper critical field, and power-law temperature dependence of the *c*-axis electrical resistance. Our results clearly demonstrate a unique method of studying a sensitive energy scale relevant to magnetic quantum criticality in UTe_2.

Results and discussion

Figure 1 presents the applied pressure dependence of $R(T)$ in UTe_2 with electrical currents applied along the crystallographic *c*-axis. The measured single-crystal sample was grown by the chemical vapor transport method, showing a residual resistance ratio (RRR) of $R(280K)/R(0K) = 5.6$ and zero-resistance state at $T_c = 1.6$ K at ambient pressure (see "Methods" section for detail). In the absence of applied pressure (0 kbar), *the* $R(T)$ curve exhibits the characteristic *c*-axis peak around 13 K as shown previously[14], which monotonically moves toward lower temperatures with increasing applied pressures while T_c increases as reported previously[25,26], reaching a maximum at $p = 9.7$ kbar (0.97 GPa) before decreasing rapidly. The resistive superconducting transition itself exhibits distinct features that evolve with pressure as shown in Fig. 1b. First, a small upturn appears just above the superconducting transition at pressures up to 9.7 kbar, which seemingly evolves from the relatively flat resistance at 0 kbar. A similar upturn was observed in prior electrical transport measurements with current applied in the (011) plane[9]. We note that the hysteresis behavior, previously observed in ref. 9, was not observed in this configuration in any *H-p-T* space studied in this work. Second, the superconducting transition narrows and becomes sharpest at $p = 9.7$ kbar, before broadening at higher pressures with a long tail just before the first-order transition to a magnetic phase occurs near $p = 14.2$ kbar (1.42 GPa). This feature was also observed previously[9], and was shown to sharpen upon application of a magnetic field. At higher pressures, the peak in $R(T)$ is diminished and a considerable increase in resistance occurs on cooling before an abrupt drop to finite resistance at the lowest measured temperatures. The low-temperature features found above 15 kbar have been previously associated with magnetic ordering[16,26].

The pressure-temperature phase diagram extracted from our *c*-axis resistivity measurements is presented in Fig. 1c as a contour plot, comparing the evolution of the resistivity magnitude with that of other measured quantities. The 3D surface plots of $R(T, p)$ are available in Supplementary Fig. 2. The precise resistivity measurements tracking the properties of the peak offer a clear picture, particularly near the critical pressure. The zero-pressure *c*-axis peak decreases in temperature with increasing pressure at a rate of -0.6 K kbar^{-1}, and the peak becomes narrower with pressure. Interestingly, the observed pressure-suppression rate of the peak is in excellent agreement with that observed for the *a*-axis magnetic susceptibility χ_a, which is -0.58 K kbar^{-1} [16]. Furthermore, Willa et al.[15] estimated the pressure-suppression rate of the minimum thermal expansion coefficient along the *c*-axis from the thermodynamic Grüneisen parameter to be -0.4 K kbar^{-1}, which also tracks the resistivity features as shown in Fig. 1c. Evidently, the pressure evolution of the *c*-axis peak closely tracks both the χ_a feature as well as the Grüneisen parameter, strongly suggesting all features have a common magnetic origin with an energy scale associated (inversely) with the strength of the fluctuation spectrum. The observed relationship between a decreasing magnetic energy scale and strengthened superconductivity is consistent with a competitive relation, supporting the picture of magnetically mediated superconductivity in UTe_2.

Applying a magnetic field at each applied pressure reveals the field evolution of $R(T)$ from 5.3 kbar to 14.2 kbar, where the *c*-axis peak remains as a pronounced local maximum but is strongly tuned by the magnetic field.

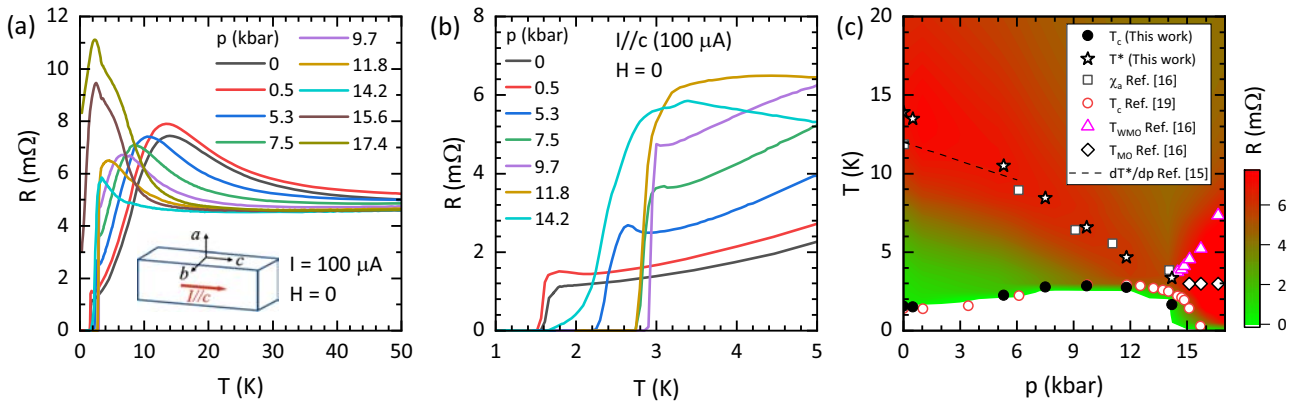

Fig. 1 | Pressure evolution of the *c*-axis resistivity of UTe_2. a shows resistance R of UTe_2 measured with the electrical current applied along the crystallographic *c*-axis under various applied pressures up to $p = 17.4$ kbar (1.74 GPa). The schematic illustrates the electrical current I (red) direction with respect to the sample orientation (blue cuboid), see also Supplementary Fig. 1. The peak in $R(T)$ monotonically moves toward the lower temperature with increasing pressure. The pressure evolution of the resistive superconducting transition is shown in (**b**) for pressure up to 14.2 kbar, above which zero resistance is not observed. **c** exhibits a phase diagram of the characteristic temperature scales (various symbols) of the system overlaid on a color contour presentation of the resistance R variation with pressure and temperature. The black (this work) and red[19] circles represent the superconducting transition and the open squares indicate a shoulder-like feature observed in magnetic susceptibility χ_a[16], which closely tracks the position of the maximum in *c*-axis resistivity (T^*) plotted as open stars. The dashed line represents the suppression of the observed minimum of the thermal expansion coefficient, estimated by using a thermodynamic relationship of electronic Grüneisen parameter[15], and the triangle and diamond symbols observed above 14.2 kbar are features attributed to magnetic ordering[16,19].

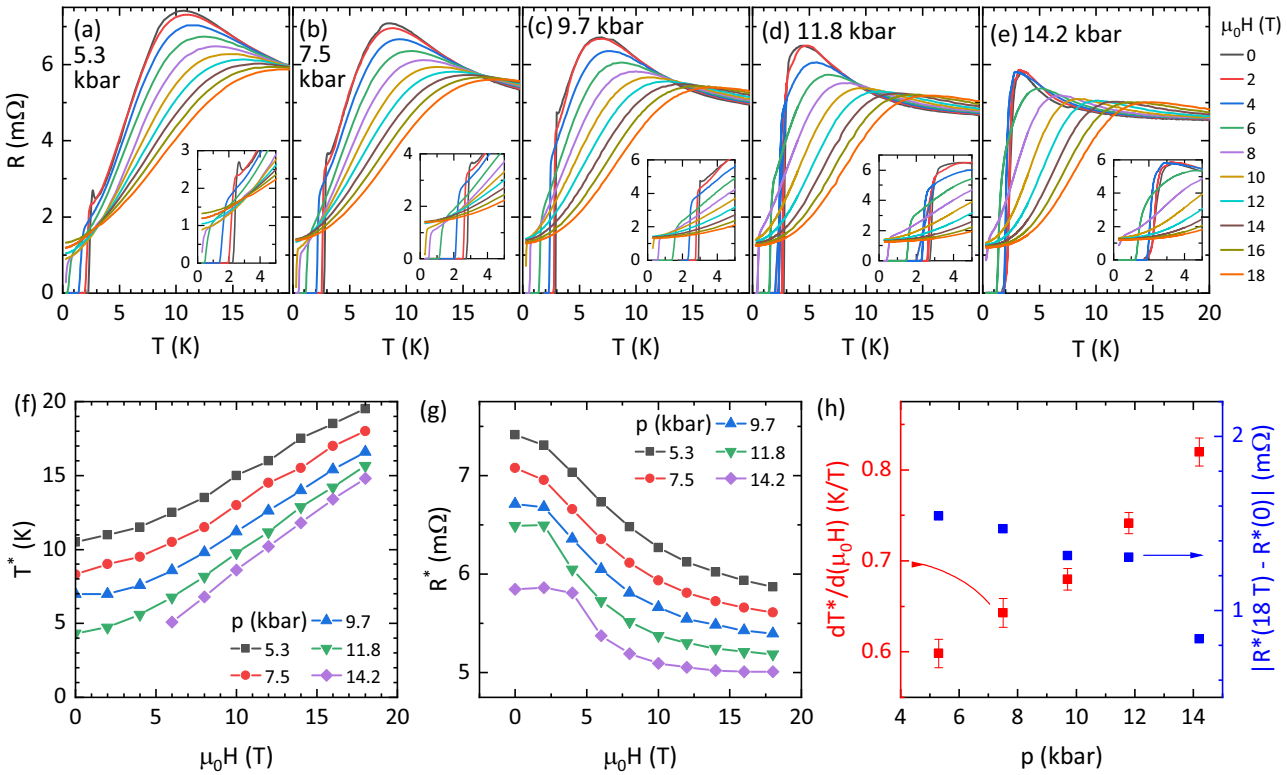

Fig. 2 | Magnetic field evolution of *c*-axis resistivity of UTe_2 under applied pressure. a–e show the field evolution of $R(T)$ with applied pressure and fields applied along the *a*-axis, in the temperature range where the data exhibit a peak that evolves very sensitively with both pressure and magnetic field. Defining T^* and R^* as, respectively, the temperature and resistance at the maximum in $R(T)$, **f–g** show the field dependence of these characteristic values to exhibit common features under all applied pressures. The numerical values of T^* presented in (**f**) are available in Supplementary Table I. The pressure evolution of the rate of increase of T^* with field, dT^*/dH, is plotted in (**h**) (left vertical axis), together with the total field variation of R^*, $|R^*(18\ \mathrm{T}) - R^*(0)|$ (right vertical axis).

The schematic of the sample with the directions of current and field is presented in Supplementary Fig. 1. As shown in Fig. 2a–e, increasing the magnetic field broadens the *c*-axis peak and increases its temperature position, while also invoking a shallower temperature dependence of the resistance with increased curvature. The broadening of the peak with the field is similar to what was observed previously at ambient pressure[27], but is contrary to the opposite trend observed with the field applied along the magnetic hard axis (*b*-axis)[27,28]. To characterize this trend, we define T^* and R^* as, respectively, the temperature and resistance values at the *c*-axis peak for each pressure and field value, with the latter representing the field evolution of the absolute low-temperature scattering rate at each pressure. We note that the asymmetric nature of the *c*-axis peak, which is likely due to a convolution of scattering rates with different profiles (e.g., spin fluctuations and phonons), makes the precise determination of its field evolution difficult. The similar broadening caused by increasing field and decreasing pressure suggests an intrinsic characteristic temperature scale that can be used for analysis. Furthermore, its near-equal evolution with the measured susceptibility feature in Fig. 1c suggests it has a common origin. The field-dependent T^* and R^* values show common features under all applied pressures with $H \| a$, as shown in Fig. 2f–g. While T^* increases with increasing field and approaches a linear trend, R^* generically decreases with increasing field, except for a saturated evolution at low fields in the vicinity of the magnetic order transition. The trends are characterized by plotting the rate $dT^*/d(\mu_0 H)$ (determined between 6 T and 18 T) and $|R^*(18\mathrm{T}) - R^*(0)|$ in Fig. 2h, which show nearly linear increase and decrease with pressure, respectively. The observed field dependence of T^* is in stark contrast to the case with $H \| b$[28], which narrows and shifts the peak to lower temperatures on the increasing field. Together with previous work[27,28], our results may support a recent $5f^2$ crystal-field model[29] that predicts the Schottky-like features observed in transport and thermodynamic quantities, assuming an anisotropic Zeeman interaction where the energy separation depends on the field orientation, and inelastic scattering that is proportional to the population of the excited spin states. The coupling coefficient of the magnetic energy with pressure can be deduced from our experiments presented in Fig. 1, and it is 0.6 K kbar^{-1} at ambient pressure, which is consistent with a thermodynamic consideration[15]. The coupling coefficient with the magnetic field can be inferred from Fig. 2h, which is 0.6 K T^{-1} and 0.83 K T^{-1} at 5.3 kbar and 14.5 kbar, respectively.

The application of pressure also affects the upper critical field $H_{c2}(T)$ by inducing an unusual low-temperature non-monotonic increase of $H_{c2}(T)$ at pressures of 5.3 kbar and higher, and reentrant behavior at 14.2 kbar as shown in Fig. 3a. The $H_{c2}(T)$ curves were determined from $R(T)$ measurements with the electrical current along the *c*-axis and the magnetic field applied parallel to the *a*-axis under applied pressure up to $p = 14.2$ kbar. We used the zero-resistance criteria for the superconducting transition temperature T_{sc} in the field. While the $H_{c2}(T)$ curve without the applied pressure exhibits a smooth variation, the application of pressure drastically changes the shape of the superconducting H-T phase lines. Near T_c, the slope of $H_{c2}(T)$ increases by almost five-fold under $p = 9.7$ kbar, and it slightly decreases at 11.8 kbar, see Fig. 3c, consistent with the previous results[17,25]. As was shown previously[9], the application of 14.2 kbar induces reentrant behavior of superconductivity. The large slope change of $H_{c2}(T)$ at T_c with pressure indicates a significant variation in the orbital limiting $H_{c2}(0)$[30]. However, the overall observed $H_{c2}(T)$ at the lowest temperature remains between 6 and 10 T as shown in Fig. 3a. When the field-driven superconducting to normal state transition occurs due to the orbital limiting effect, $H_{c2}(0)$ can be estimated from the slope of $H_{c2}(T)$ at T_c with a relation, $H_{HW} = -\lambda T_c H'_{c2}(T_c)$, proposed by Helfand and Werthamer (HW)[30]. Here $\lambda \approx 0.73$ and 0.69, which correspond to the clean and dirty limits, respectively[30,31]. Alternatively, spin-singlet superconductivity can be suppressed due to the Zeeman energy contribution of Pauli paramagnetism, and the limiting value H_P can be estimated by the relation, $H_P = \Delta_0/\sqrt{2}\mu_B$.

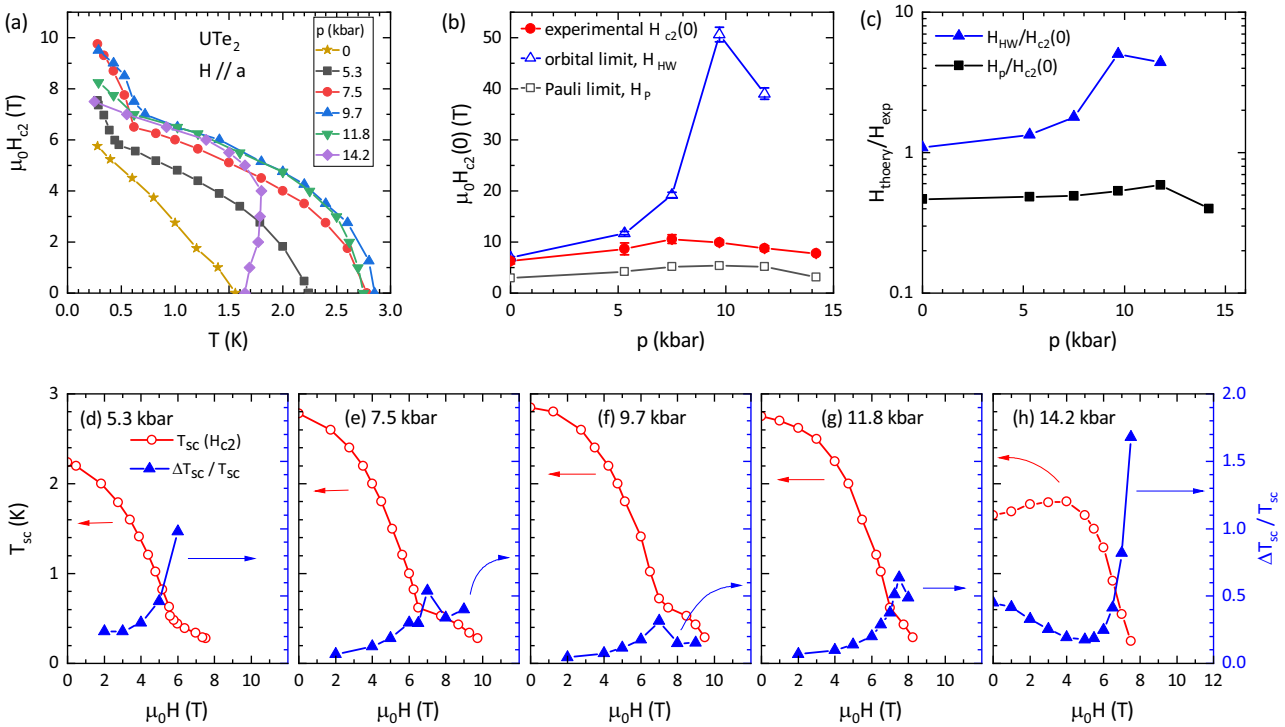

Fig. 3 | Superconducting upper critical fields of UTe_2 as a function of applied pressure. a shows the temperature-dependent upper critical field $H_{c2}(T)$ under various applied pressures with a field H applied along the a-axis. We used the zero-resistance criteria for the superconducting transition temperature T_{sc} in a magnetic field. **b** compares the extracted zero-temperature experimental $H_{c2}(0)$ values (red circles) to the calculated orbital limiting field, H_{HW} (blue triangles), and the paramagnetic limiting field, H_P (black squares). See text for definitions of H_{HW} and H_P. The experimental $H_{c2}(0)$ values are determined by extrapolating the $H_{c2}(T)$ curves to zero temperature. The numerical values of the presented data in (**a**–**c**) are available in Supplementary Table 2. **c** shows the pressure evolution of $H_{HW}/H_{c2}(0)$ and $H_P/H_{c2}(0)$. **d**–**h** present the relation between the anomalous behavior $H_{c2}(T)$ (red circles) and the width of the superconducting phase transition $\Delta T_{sc}/T_{sc}$ (blue triangles).

Here Δ_0 and μ_B are the magnitudes of the superconducting energy gap at zero temperature and the Bohr magneton, respectively. For a weak-coupling Bardeen-Cooper-Schrieffer superconductor, $\mu_0 H_P = \alpha T_c$ where $\alpha \approx 1.87$ T K^{-1} [32], which is consistent with the gap energy of $\Delta_0 \sim 0.25$ meV observed in scanning tunnel microscopy experiments[33].

We compare the experimental $H_{c2}(0)$ to both limiting fields, H_{HW} and H_P, in Fig. 3b. We note that H_{HW} is ill-defined under 14.2 kbar because of the reversed sign of $H'_{c2}(T_c)$, i.e., reentrant superconductivity. Figure 3c shows the pressure evolution of $H_{HW}/H_{c2}(0)$ and $H_P/H_{c2}(0)$. While H_P remains less than $H_{c2}(0)$, indicating non-singlet pairing, H_{HW} exhibits a substantial variation. The large H_{HW} prediction is generally evidence for the heavy-fermion normal state[34]. The pressure evolution of H_{HW}, which exhibits a significant enhancement around 10 kbar, indicates increasing effective mass with pressure. However, the orbital limiting effect is interrupted, and the largest discrepancy between $H_{c2}(0)$ and H_{HW} is observed at 9.7 kbar where the highest T_c is observed. A similar effect was observed in other heavy-fermion superconductors near quantum criticality[34], suggesting the existence of a QCP near 10 kbar (1 GPa). At low temperatures, a drastic slope change appears under pressure between 5.3 and 11.8 kbar. The slope change in UTe_2 was previously reported by Aoki et al., which was attributed to the existence of other superconducting phases[25]. Similar $H_{c2}(T)$ behavior was reported by Kasahara et al. in FeSe[35], which was attributed to the Fulde–Ferrell–Larkin–Ovchinnikov (FFLO) state[36–38].

We found the width of the superconducting phase transition in resistivity is closely related to this anomalous behavior in $H_{c2}(T)$. To shed light on the origin of this feature, we determined the field-dependent transition width compared to the T_{sc} that is determined at zero resistivity, $\Delta T_{sc}/T_{sc}$. For all studied pressures, $\Delta T_{sc}/T_{sc}$ exhibits strong enhancement where the sudden slope change occurs as shown in Fig. 3d–h. Defining H^* as the field value where the slope of $H_{c2}(T)$ changes, we observe that $\Delta T_{sc}/T_{sc}$ decreases above H^* under $p = 7.5, 9.7, 11.8$ kbar where the low-temperature data above H^* are available. A broad superconducting transition is usually associated with inhomogeneity[19,39,40] or a filamentary superconducting state. However, the systematic field dependence rules out these simple scenarios, suggesting this is rather associated with the competing order parameters and quantum criticality leading to anomalous transport properties.

Whereas Fermi liquid behavior is routinely manifested in normal metals as a quadratic temperature dependence of resistivity due to electron-electron scattering, a sub-quadratic exponent is a well-known signature of unconventional scattering usually attributed to strong spin fluctuations near a magnetic quantum critical point[1,2,11–13,34]. Below, we investigate the field and pressure evolution of the power-law temperature dependence of ρ_c in UTe_2. Because of the limited temperature range between T_c and T^*, we employ a double-logarithm fitting routine commonly used[9,26] to produce contour plot phase diagrams to display the general trends as well as power-law fits to $R(T) = R(0) + AT^n$ to study the trends with field and pressure. Figure 4a–e present the phase diagrams for each applied pressure determined by the field-dependent exponent n^* of $R(T)$ determined using the relation $n^* = d[\log(R(T) - R_0)]/d[\log T]$. R_0 is the residual resistance at $T = 0$ and is estimated by extrapolating the $R(T)$ tail assuming a power-law behavior of $R(T)$ in the low-temperature limit. Provided R_0 is accurately determined, n^* is equivalent to the power-law exponent n in $R(T) = R_0 + AT^n$, yielding a continuous approximate measure of the temperature power-law exponent of $R(T)$. In previous reports, the a-axis resistivity of UTe_2 was shown to remain quadratic in temperature (i.e., $\Delta\rho_a \sim AT^n$, with $n = 2$) for magnetic fields applied along both a- and b-axes up to 40 T, with the coefficient A significantly enhanced near a 35 T b-axis field[41] but retaining Fermi liquid (FL) behavior. Linear in temperature (i.e., $n = 1$) resistivity was reported by Thomas et al.[26] in the a-axis transport at low temperatures around 13 kbar. For c-axis resistivity, Eo et al. reported

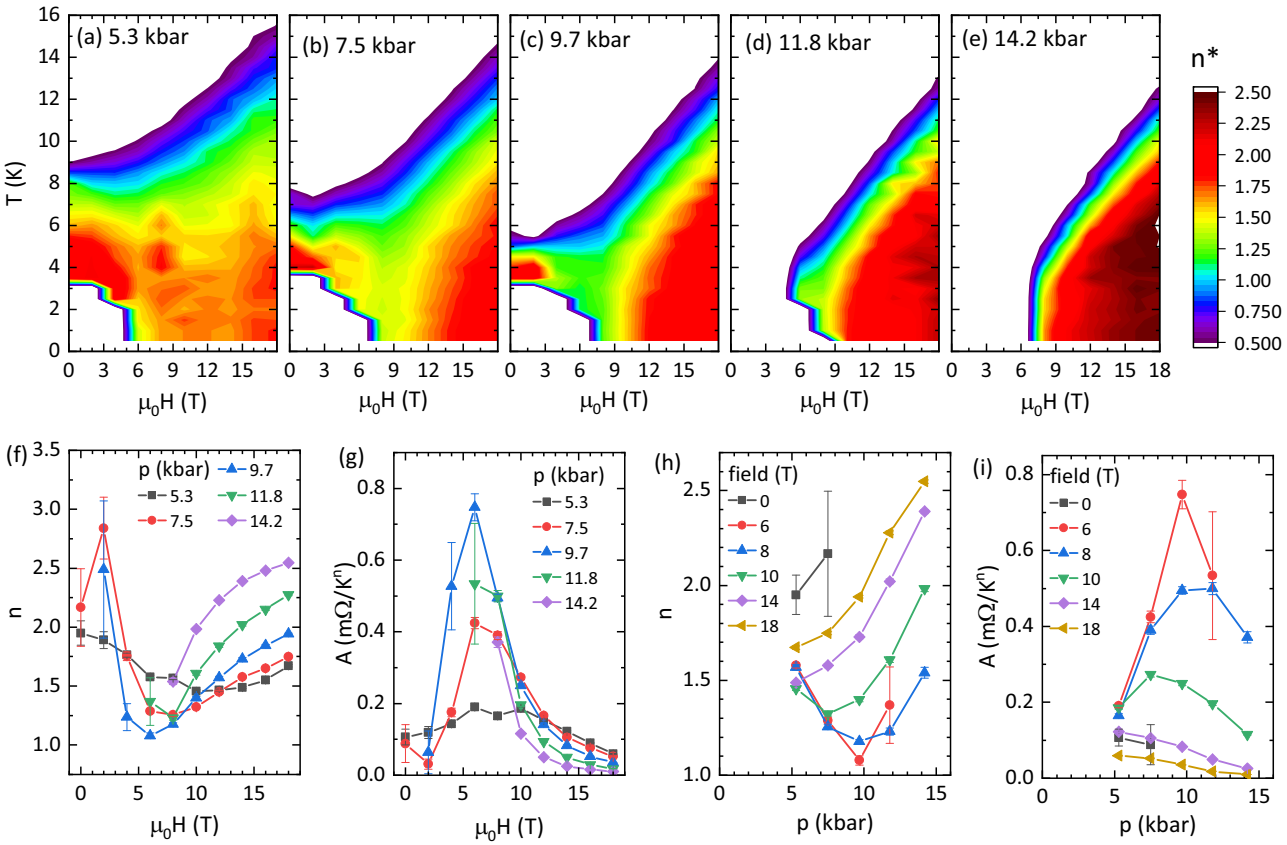

Fig. 4 | Evolution of non-Fermi liquid behavior with field and pressure in UTe_2. **a**–**e** show the field-dependent exponent n^*, representative of the power-law exponent of the temperature dependence of *c*-axis resistance $R(T)$ for fields applied along the *a*-axis, determined using the relation $n^* = d[\log(R(T) - R_0)]/d[\log T]$. At 5.3 kbar, n^* exhibits Fermi Liquid behavior (i.e., $n^* = 2$, shown as yellow coloring) just above T_c near zero field, but decreases toward $n^* = 1.5$ (light green) with increasing fields and decreasing temperatures. To quantify the trends, least-squares fitting of selected $R(T)$ using the relation $R(T) = R(0) + AT^n$ to the experimental data with $T \leq T^*/2$ yield values for the extracted power-law exponent n and corresponding temperature coefficient A, summarized as a function of the field in (**f**, **g**) and pressure in (**h**, **i**). The numerical values of n and A are available in Supplementary Tables 3 and 4, respectively.

quadratic FL behavior in the absence of both field and applied pressures[14]. As shown in Fig. 4, $R(T)$ exhibits the Fermi liquid behavior (red) just above T_c under 5.3 kbar in zero field, but the exponent n^* decreases toward $n^* = 1.5$ (yellow) with increasing field near $H_{c2}(0)$. Under 7.5 kbar and 9.7 kbar, while the *c*-axis transport exhibits the non-Fermi liquid behavior near $H_{c2}(0)$, the Fermi liquid behavior (red) is recovered at high fields between 15 T and 18 T. Under 11.8 kbar and 14.2 kbar, the exponent reaches $n^* = 2.5$ (brown) at high fields.

We also performed least-squares fits on selected $R(T)$ curves by fitting our data to the relation $R(T) = R(0) + AT^n$ with $T \leq T^*/2$ well away from the *c*-axis peak, selecting pressure and field values with the widest temperature ranges available. The field evolution of n and A are summarized in Fig. 4f, g, and pressure evolution in Fig. 4h, i. For $p = 5.3$ kbar, $n = 2$ in zero field but smoothly decreases with increasing field, showing a minimum value of $n = 1.5$ near 10 T. It weakly increases at high fields while remaining subquadratic up to the highest fields measured. For higher pressures between 7.5 and 11.8 kbar, n exhibits a more drastic decrease with a minimum near 7 T where the $H_{c2}(T)$ changes the slope. At higher fields, n increases substantially to about 2.5 for 11 kbar and 14.2 kbar. The extracted A-coefficient appears to correlate inversely with the trends in the power-law exponent, with a dip in n and a peak in A at a field near the suppression of the superconducting state being typical for a system at or near a quantum critical point. To directly visualize the power-law evolution, we plot $R(T)$ under selected fields and pressures that exhibit the most striking non-Fermi liquid behavior in Fig. 5. It is clear that the T^2 behavior at ambient pressure (Fig. 5a) evolves rapidly as a function of pressure and magnetic field to exhibit a nearly linear behavior under $p = 9.7$ kbar and $\mu_0 H = 8$ T (Fig. 5d). Our power-law results with a unique current-field configuration can be directly compared to that reported in previous works[9,26–28], providing clear indications of quantum criticality in UTe_2.

Conclusions

In conclusion, we investigated the tuning of a magnetic energy scale with applied hydrostatic pressure and magnetic field along the *a*-axis as complementary (and opposing) tuning parameters in the heavy-fermion superconductor UTe_2 in the vicinity of a long-range magnetic ordering. Strong spin fluctuations manifest as a pronounced local maximum at low temperatures, which is identified as a peak in the *c*-axis electrical transport. Upon increasing pressure, the characteristic *c*-axis peak moves to a lower temperature before vanishing near the critical pressure of 15 kbar (1.5 GPa). The application of a magnetic field shifts the peak to a higher temperature and broadens the peak under all studied pressure values. The power-law behavior of the *c*-axis transport is also significantly affected by the application of pressure and field where the non-Fermi liquid behavior is most pronounced around 9.7 kbar and 7 T, exhibiting nearly linear in temperature resistivity and an enhanced pre-factor. These signatures in *c*-axis transport are a revealing indication of an incipient magnetic order that has a strong influence on the physical properties and possibly superconductivity. Our results provide a measurement of the

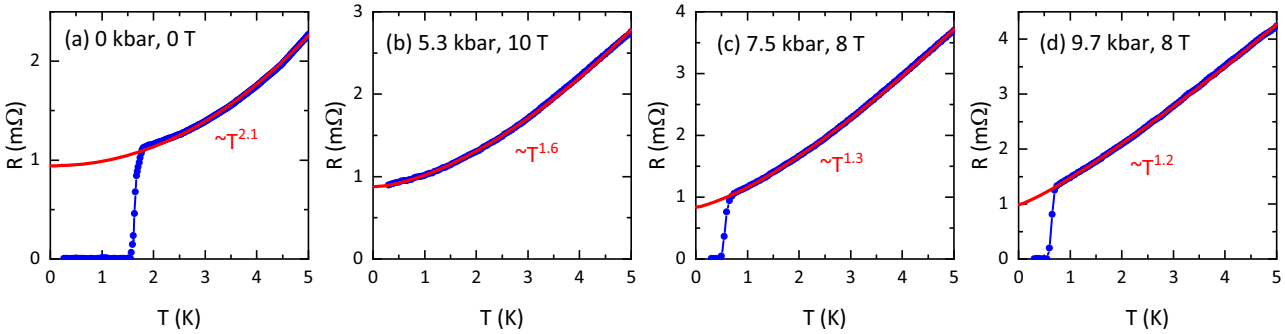

Fig. 5 | Evolution of the power-law behavior in $R(T)$ in UTe_2. Power-law behavior in a magnetic field and under pressure is shown for **a** 0 kbar with 0 T, **b** 5.3 kbar with 10 T, **c** 7.5 kbar with 8 T, and **d** 9.7 kbar with 8 T. The direct comparison between (0 kbar, 0 T) and (9.7 kbar, 8 T) curves can be found in Supplementary Fig. 3.

pressure and field evolution of the magnetic energy scale relevant to quantum criticality in UTe_2 and shed light on its influence on unconventional superconductivity.

Methods

Sample preparation

Single crystals of UTe_2 were synthesized by the chemical vapor transport method using iodine as the transport agent. Elements of U and Te with an atomic ratio of 2:3 were sealed in an evacuated quartz tube, together with 3 mg cm^{-3} iodine. The ampoule was gradually heated up and held in the temperature gradient of 1060/1000 °C for 7 days, after which it was furnace-cooled to room temperature. Samples used in this study were obtained from the same synthesis batch as used in the study of Hayes et al.[42].

Transport measurements under pressure

A UTe_2 single-crystal sample with an onset $T_c \approx 1.78$ K was prepared for transport measurements by soldering electrical leads with gold wires. The typical contact resistance is less than 1 Ω. The transport data were taken with a fixed current of 100 μA. A nonmagnetic piston-cylinder pressure cell was used for measurements under pressure up to 17.4 kbar, with Daphne oil 7373 as the pressure medium. Transport measurements were performed in a commercial ^{3}He cryostat system with a base temperature of 300 mK, which is equipped with a superconducting magnet. The current was applied along the crystallographic c-axis. The RRR of the sample used in the current study is $R(280\,\mathrm{K})/R(2.2\,\mathrm{K}) = 4.27$ or $R(280\,\mathrm{K})/R(0\,\mathrm{K}) = 5.57$. Here $R(0\,\mathrm{K})$ was determined by extrapolating with a power-law function, $R(T) = R(0\,\mathrm{K}) + AT^n$. The magnetic field up to 18 T was applied along the a-axis, perpendicular to the current. The pressure produced on the single-crystal sample at low temperatures was calibrated by measuring the superconducting transition temperature of lead placed in the cell. The known pressure dependencies of the superconducting transition temperature of Pb[9,43] were used for this purpose.

Data availability

The data that support the findings of this study are available from the corresponding authors upon request.

Received: 17 October 2023; Accepted: 2 December 2024;
Published online: 08 January 2025

References

1. Mathur, N. D. et al. Magnetically mediated superconductivity in heavy fermion compounds. *Nature* **394**, 39 (1998).
2. Paglione, J. et al. Field-induced quantum critical point in $CeCoIn_5$. *Phys. Rev. Lett.* **91**, 246405 (2003).
3. Stockert, O. & Steglich, F. Unconventional quantum criticality in heavy-fermion compounds. *Annu. Rev. Condens. Matter Phys.* **2**, 79 (2011).
4. Shibauchi, T., Carrington, A. & Matsuda, Y. A quantum critical point lying beneath the superconducting dome in iron pnictides. *Annu. Rev. Condens. Matter Phys.* **5**, 113 (2014).
5. Aoki, D., Ishida, K. & Flouquet, J. Review of U-based ferromagnetic superconductors: Comparison between UGe_2, URhGe, and UCoGe. *J. Phys. Soc. Jpn.* **88**, 022001 (2019).
6. Ran, S. et al. Nearly ferromagnetic spin-triplet superconductivity. *Science* **365**, 684 (2019).
7. Rosa, P. F. S. et al. Single thermodynamic transition at 2 K in superconducting UTe_2 single crystals. *Commun. Mater.* **3**, 33 (2022).
8. Kang, B., Choi, S. & Kim, H. Orbital selective Kondo effect in heavy fermion superconductor UTe_2. *npj Quantum Mater.* **7**, 64 (2022).
9. Ran, S. et al. Enhancement and reentrance of spin triplet superconductivity in UTe_2 under pressure. *Phys. Rev. B* **101**, 140503 (2020).
10. Knafo, W. et al. Incommensurate antiferromagnetism in UTe_2 under pressure. Preprint at https://arxiv.org/abs/2311.05455 (2023).
11. Si, Q. & Steglich, F. Heavy fermions and quantum phase transitions. *Science* **329**, 1161 (2010).
12. Keimer, B., Kivelson, S. A., Norman, M. R., Uchida, S. & Zaanen, J. From quantum matter to high-temperature superconductivity in copper oxides. *Nature* **518**, 179 (2015).
13. Paglione, J. & Greene, R. L. High-temperature superconductivity in iron-based materials. *Nat. Phys.* **6**, 645 (2010).
14. Eo, Y. S. et al. c-axis transport in UTe_2: evidence of three-dimensional conductivity component. *Phys. Rev. B* **106**, L060505 (2022).
15. Willa, K. et al. Thermodynamic signatures of short-range magnetic correlations in UTe_2. *Phys. Rev. B* **104**, 205107 (2021).
16. Li, D. et al. Magnetic properties under pressure in novel spin-triplet superconductor UTe_2. *J. Phys. Soc. Jpn.* **90**, 073703 (2021).
17. Knebel, G. et al. Anisotropy of the upper critical field in the heavy-fermion superconductor UTe_2 under pressure. *J. Phys. Soc. Jpn.* **89**, 053707 (2020).
18. Cairns, L. P., Stevens, C. R., O'Neill, C. D. & Huxley, A. Composition dependence of the superconducting properties of UTe_2. *J. Phys.: Condens. Matter* **32**, 415602 (2020).
19. Thomas, S. M. et al. Spatially inhomogeneous superconductivity in UTe_2. *Phys. Rev. B* **104**, 224501 (2021).
20. Tokunaga, Y. et al. ^{125}Te-NMR study on a single crystal of heavy fermion superconductor UTe_2. *J. Phys. Soc. Jpn.* **88**, 073701 (2019).
21. Niu, Q. et al. Fermi-surface instability in the heavy-fermion superconductor UTe_2. *Phys. Rev. Lett.* **124**, 086601 (2020).
22. Duan, C. et al. Incommensurate spin fluctuations in the spin-triplet superconductor candidate UTe_2. *Phys. Rev. Lett.* **125**, 237003 (2020).
23. Duan, C. et al. Resonance from antiferromagnetic spin fluctuations for superconductivity in UTe_2. *Nature* **600**, 636 (2021).
24. Butch, N. P. et al. Symmetry of magnetic correlations in spin-triplet superconductor UTe_2. *npj Quantum Mater.* **7**, 39 (2022).

25. Aoki, D. et al. Multiple superconducting phases and unusual enhancement of the upper critical field in UTe_2. *J. Phys. Soc. Jpn.* **89**, 053705 (2020).
26. Thomas, S. M. et al. Evidence for a pressure-induced antiferromagnetic quantum critical point in intermediate-valence UTe_2. *Sci. Adv.* **6**, eabc8709 (2020).
27. Thebault, T. et al. Anisotropic signatures of electronic correlations in the electrical resistivity of UTe_2. *Phys. Rev. B* **106**, 144406 (2022).
28. Knebel, G. et al. *c*-axis electrical transport at the metamagnetic transition in the heavy-fermion superconductor UTe_2 under pressure. *Phys. Rev. B* **109**, 155103 (2024).
29. Khmelevskyi, S., Pourovskii, L. V. & Tereshina-Chitrova, E. A. Structure of the normal state and origin of the Schottky anomaly in the correlated heavy-fermion superconductor UTe_2. *Phys. Rev. B* **107**, 214501 (2023).
30. Helfand, E. & Werthamer, N. R. Temperature and purity dependence of the superconducting critical field, H_{c2}. ii. *Phys. Rev.* **147**, 288 (1966).
31. Kogan, V. G. & Prozorov, R. Orbital upper critical field and its anisotropy of clean one- and two-band superconductors. *Rep. Prog. Phys.* **75**, 114502 (2012).
32. Tinkham, M. *Introduction to Superconductivity,* 2nd Edition (Dover Publications, 2004).
33. Jiao, L. et al. Chiral superconductivity in heavy-fermion metal UTe_2. *Nature* **579**, 523 (2020).
34. Stewart, G. R. Heavy-fermion systems. *Rev. Mod. Phys.* **56**, 755 (1984).
35. Kasahara, S. et al. Evidence for an Fulde-Ferrell-Larkin-Ovchinnikov state with segmented vortices in the BCS-BEC-crossover superconductor FeSe. *Phys. Rev. Lett.* **124**, 107001 (2020).
36. Fulde, P. & Ferrell, R. A. Superconductivity in a strong spin-exchange field. *Phys. Rev.* **135**, A550 (1964).
37. Larkin, A. I. & Ovchinnikov, Y. N. Nonuniform state of superconductors. *Zh. Eksp. Teor. Fiz.* **47**, 1136 (1964).
38. Matsuda, Y. & Shimahara, H. Fulde–Ferrell–Larkin–Ovchinnikov state in heavy fermion superconductors. *J. Phys. Soc. Jpn.* **76**, 051005 (2007).
39. Casalbuoni, R. & Nardulli, G. Inhomogeneous superconductivity in condensed matter and QCD. *Rev. Mod. Phys.* **76**, 263 (2004).
40. Park, T. et al. Textured superconducting phase in the heavy fermion $CeRhIn_5$. *Phys. Rev. Lett.* **108**, 077003 (2012).
41. Knafo, W. et al. Magnetic-field-induced phenomena in the paramagnetic superconductor UTe_2. *J. Phys. Soc. Jpn.* **88**, 063705 (2019).
42. Hayes, I. M. et al. Multicomponent superconducting order parameter in UTe_2. *Science* **373**, 797 (2021).
43. Smith, T. F. & Chu, C. W. Will pressure destroy superconductivity? *Phys. Rev.* **159**, 353 (1967).

Acknowledgements

The authors are grateful for the useful discussions with Andriy Nevidomskyy. Research at the University of Maryland was supported by the Department of Energy Award No. DE-SC-0019154 (transport experiments), the Gordon and Betty Moore Foundation's EPiQS Initiative through Grant No. GBMF9071 (materials synthesis), NIST, and the Maryland Quantum Materials Center.

Author contributions

J.P. and N.P.B. designed the project. H.K. and I.L. performed transport measurements. N.P.B. and S.R. synthesized materials. H.K., W.L., and Y.S.E. analyzed data. H.K. and J.P. wrote the paper with contributions from all authors.

Competing interests

The authors declare no competing interests.

Additional information

Supplementary information The online version contains supplementary material available at https://doi.org/10.1038/s43246-024-00713-y.

Correspondence and requests for materials should be addressed to Hyunsoo Kim or Johnpierre Paglione.

Peer review information *Communications materials* thanks the anonymous reviewers for their contribution to the peer review of this work. Primary Handling Editor: Aldo Isidori. A peer review file is available.

Supplementary Information for "Tuning a magnetic energy scale with pressure and field in UTe_2"

Hyunsoo Kim,[1,2] I-Lin Liu,[2] Wen-Chen Lin,[2] Yun Suk Eo,[2]
Sheng Ran,[2] Nicholas P. Butch,[2,3] and Johnpierre Paglione[2,4]

[1]*Department of Physics, Missouri University of Science and Technology, Rolla, MO 65409, USA*

[2]*Maryland Quantum Materials Center and Department of Physics, University of Maryland, College Park, Maryland, USA*

[3]*NIST Center for Neutron Research, National Institute of Standards and Technology, Gaithersburg, MD 20899, USA*

[4]*Canadian Institute for Advanced Research, Toronto, Ontario M5G 1Z8, Canada*

Corresponding authors:
Johnpierre Paglione (paglione@umd.edu),
Hyunsoo Kim (hyunsoo.kim@mst.edu)

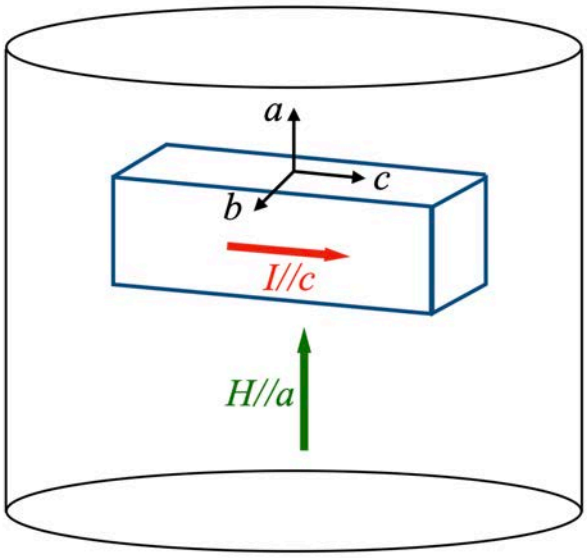

Supplementary Figure 1. Illustration of sample orientation (blue cuboid) with respect to the electrical current I (red) and magnetic field H (green) in a inner volume of a piston clamp pressure cell, represented by a cylinder.

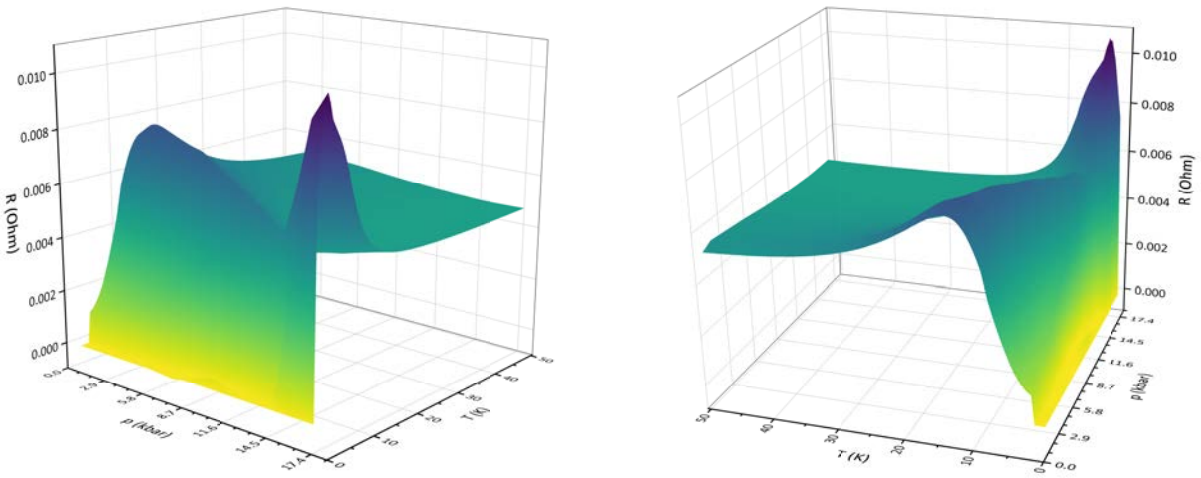

Supplementary Figure 2. 3D surface plots of $R(T, p)$ in UTe_2 with the electric current along the c-axis in two different viewing perspectives.

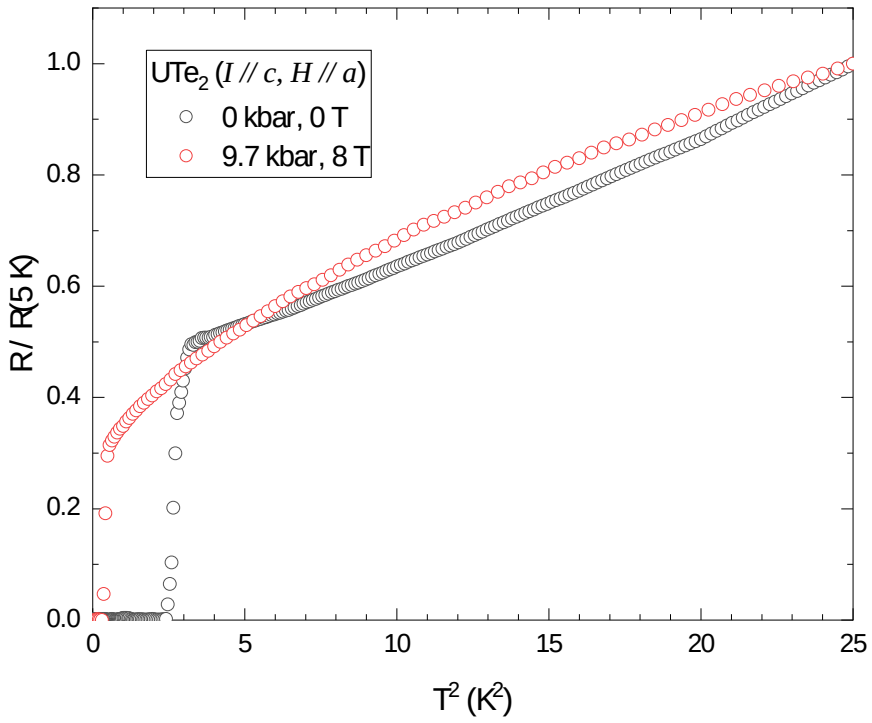

Supplementary Figure 3. Comparison of the power-law behavior in UT_2 with $I \parallel c$ and $H \parallel a$. The Fermi liquid behavior T^2 at ambient pressure and zero magnetic field becomes nearly linear resistivity in temperature under 9.7 kbar and 8 T (see main text for details).

$\mu_0 H$ [T]	5.3 kbar	7.5 kbar	9.7 kbar	11.8 kbar	14.2 kbar
0	10.5	8.3	6.99	4.34	
2	11	9	6.99	4.74	
4	11.5	9.5	7.59	5.59	
6	12.5	10.5	8.58	6.76	5.1
8	13.5	11.5	9.8	8.17	6.8
10	15	13	11.2	9.78	8.6
12	16	14.5	12.6	11.19	10.2
14	17.5	15.5	14	12.88	11.8
16	18.5	17	15.4	14.2	13.4
18	19.5	18	16.6	15.68	14.8

Supplementary Table 1. Field- and pressure-dependent c-axis peak position T^* presented in Fig. 2 in the main text. The temperature values are presented in Kelvin.

p [kbar]	T_c [K]	$\mu_0 dH_{c2}/dT$ [T/K]	$\mu_0 H_{c2}(0)$ [T]	$\mu_0 H_{HW}$ [T]	$\mu_0 H_P$ [T]
0	1.56	-6.25	6.3 ± 0.5	6.9 ± 0.2	2.9
5.3	2.24	-7.38	8.7 ± 1.1	11.7 ± 0.3	4.2
7.5	2.78	-9.72	10.6 ± 0.8	19.2 ± 0.5	5.2
9.7	2.85	-25.0	10.0 ± 0.5	51.0 ± 1.4	5.3
11.8	2.75	-20.0	8.8 ± 0.5	39.1 ± 1.1	5.1
14.2	1.65			7.8 ± 0.3	3.1

Supplementary Table 2. The superconducting critical temperature and upper critical fields. $H_{c2}(0)$ is determined from experimental values by extrapolating to $T = 0$, and H_{HW} and H_P are theoretical estimates, see main text for details.

$\mu_0 H$ [T]	5.3 kbar	7.5 kbar	9.7 kbar	11.8 kbar	14.2 kbar
0	1.95 ± 0.10	2.17 ± 0.33			
2	1.89 ± 0.07	2.84 ± 0.26	2.49 ± 0.58		
4	1.76 ± 0.02	1.75 ± 0.04	1.24 ± 0.11		
6	1.58 ± 0.01	1.29 ± 0.02	1.08 ± 0.02	1.37 ± 0.20	
8	1.57 ± 0.01	1.26 ± 0.01	1.18 ± 0.01	1.23 ± 0.02	1.54 ± 0.03
10	1.46 ± 0.01	1.32 ± 0.01	1.40 ± 0.01	1.61 ± 0.02	1.98 ± 0.01
12	1.46 ± 0.01	1.45 ± 0.01	1.57 ± 0.01	1.84 ± 0.01	2.23 ± 0.01
14	1.49 ± 0.01	1.58 ± 0.01	1.73 ± 0.01	2.02 ± 0.01	2.39 ± 0.01
16	1.55 ± 0.01	1.65 ± 0.01	1.84 ± 0.01	2.15 ± 0.01	2.48 ± 0.01
18	1.67 ± 0.01	1.75 ± 0.01	1.94 ± 0.01	2.28 ± 0.01	2.55 ± 0.01

Supplementary Table 3. Power-law exponent n determined from the least square fitting of AT^n with temperatures up to $T^*/2$. The coefficient A is presented in Supplementary Table 4.

$\mu_0 H$ [T]	5.3 kbar	7.5 kbar	9.7 kbar	11.8 kbar	14.2 kbar
0	107.0 ± 21.9	88.1 ± 52.6			
2	119.0 ± 17.0	31.0 ± 13.9	63.8 ± 59.4		
4	142.7 ± 4.9	175.1 ± 11.9	527.0 ± 121.9		
6	190.7 ± 4.9	424.6 ± 15.4	747.7 ± 37.6	533.7 ± 168.4	
8	164.7 ± 4.8	389.8 ± 10.9	494.6 ± 10.1	499.6 ± 16.0	370.8 ± 14.8
10	186.0 ± 4.4	273.0 ± 6.1	249.5 ± 5.7	196.7 ± 4.9	116.0 ± 2.4
12	153.3 ± 3.1	166.4 ± 3.8	141.2 ± 3.7	94.0 ± 2.2	50.0 ± 0.8
14	122.4 ± 2.2	105.3 ± 2.3	82.6 ± 1.8	49.8 ± 1.1	25.5 ± 0.5
16	89.6 ± 1.8	75.9 ± 1.6	52.7 ± 1.0	29.3 ± 0.5	15.4 ± 0.3
18	59.1 ± 1.2	52.0 ± 0.9	35.4 ± 0.5	18.0 ± 0.3	10.1 ± 0.2

Supplementary Table 4. The power-law coefficient A in $\mu\Omega/\mathrm{K}^n$ from least square fitting of power-law where n values are presented in Supplementary Table 3.